Heat Mass Transfer (2010) 46:1261–1276
DOI 10.1007/s00231-010-0649-8

ORIGINAL

A high order control volume finite element procedure for transient heat conduction analysis of functionally graded materials

J. Charoensuk · P. Vessakosol

Received: 4 December 2009 / Accepted: 15 July 2010 / Published online: 5 August 2010

Abstract A robust unstructured control-volume finite element method is presented for the solution of two-dimensional transient heat conduction in functionally graded materials (FGMs) with isotropic properties. The material properties at a point in the domain vary exponentially to spatial coordinates. A triangular mesh is chosen for spatial discretization and a fully implicit scheme is adapted for time discretization. Several problems are investigated and the results are successfully validated by using analytical and other numerical solutions available in the literature.

1 Introduction

Functionally graded material (FGMs) is a class of composites having continuous spatial variation of material properties. This type of material has recently been used in a severe temperature environment-a body is subjected to high transient heating and cooling within a short period of time [1, 2]. With appropriate grading profile, the thermal stress, residual stress, and stress concentration factor in the structure can be reduced when compared with those in the laminated composite structures under the same loading condition. Mostly, FGMs are manufactured from isotropic components such as metals and ceramics. FGMs have become widely used not only in thermal protection purpose but also in other areas; i.e. biomedical engineering and fuel cell [3, 4].

Transient heat conduction in FGMs has been investigated by several researchers [5–12] for better understanding of these materials. Sladek et al. [9] applied a meshless method called local boundary integral equation method (LBIEM) to analyze the transient heat conduction problem in FGM. Wang et al. [10] determined the transient temperature field in FGM plate, shell and sphere by a finite element/finite difference (FE/FD) method and also considered the effect of material properties on the temperature. Wang and Tian [11] gave more details on the above FE/FD method and demonstrated their method to two-dimensional heat transfer under transient state. Wang et al. [12] proposed the virtual boundary collocation method (VBCM) for transient heat conduction analysis in FGM.

Control volume finite element method (CVFEM) is an alternative numerical technique for the solution of FGM problems. It is a combination of numerical discretization inherited from the finite volume method and numerical interpolation of FEM and sometimes referred to as a vertex-centered finite volume method [13, 25–28]. This technique has a potential for multi-physical problems such as the conjugate heat transfer where the energy balance between solid and moving fluid needed to be considered simultaneously [35]. From authors' point of view, CVFEM is applicable for the transient heat conduction problems in FGM where the non-homogenous material properties of FGM induce the non-linearity in heat conduction problem.

Early development of finite volume method had focused on the non-linearity in problems of fluid dynamics [13]. Therefore, the domain geometries initially modeled by finite volume method were relatively simple. The use of structured mesh based either on rectangular or body-fitted coordinates did not lead to severe errors in the numerical results. In modern applications, however, the domain geometries are much more complicated than those in the past. Consequently, it is difficult to handle these works with structured mesh solver. Unstructured mesh solver

J. Charoensuk (✉) · P. Vessakosol
Department of Mechanical Engineering,
Faculty of Engineering, King Mongkut's Institute of Technology
Ladkrabang, Bangkok 10520, Thailand
e-mail: kcjarruw@kmitl.ac.th

would be a promising tool for research and design in novel engineering products development. The unstructured finite volume may be roughly separated into two main groups by different definitions of control volume, the cell-centered and vertex-centered approaches. For the cell-center approach, each control volume is defined by triangular or quadrilateral mesh. The value of unknown variable, such as temperature, is referred and stored at the center of control volume. On the other hand, the vertex-centered approach starts with defining a computational node at the grid point of triangular or quadrilateral mesh and then sub-control volumes are built around it. Therefore, the control volume is built from summation of sub-control volumes. With this approach the value of unknown variable, i.e. temperature, is stored at the vertex point. Although a finite volume method have been applied on general fluid flow problems, there are some works concerning the heat conduction problem in FGM.

Early applications of the finite volume method on problems of non-homogeneous material like FGM had been carried out and reviewed by Aboudi et al. [14, 15]. They employed the two-level unit cell discretization involving generic cell and subcell levels to capture the graded material's heterogeneous microstructure. Their approach was called high-fidelity generalized method of cells (HFGMC). Bansal and Pindera [16–20] utilized the concept of local/global stiffness matrix approach for the solution of local displacement and stress fields within the repeating unit cell. They also constructed the cell problems by a standard elasticity approach involving the direct volume-averaging of the local field equations and the satisfaction of the local continuity conditions in a surface-average sense. They had named their approach as the finite volume direct average micromechanics (FVDAM). Even though the FVDAM increased the efficiency of HFGMC, the subcell discretization used by FVDAM was limited to rectangular control volume. This method was inefficient in approximating the curved boundary and produced unrealistic stress concentrations at the interface between the materials of different elastic properties. Recently, Cavalcante [21] proposed the quadrilateral subcell discretization of parametric finite-volume theory to mitigate the negative impact of rectangular subcell mentioned above. Cavalcante et al. [22, 23] applied the parametric finite-volume theory to analyze the steady and transient thermal and stress responses of FGM cylinder subjected to the thermo-mechanical loading. Their method could improve the result of stress concentration at the material interface in an eshelby problem. Gao et al. [24] directly extended the FVDAM to quadrilateral finite volume direct average micromechanics (QFVDAM). With this technique, a system of quadrilateral subcells numbering was not restricted to an order fashion like that of Cavalcante et al. [22, 23].

In contrast to the above parametric mapping approach based on quadrilateral subcell and higher order approximation, this paper adopts the finite volume formulation based on triangular unstructured mesh with quadratic interpolation function. It is similar to the commonly used higher order interpolation in the finite element method. The objective of this paper is to present a distinguish methodology derived from CVFEM for transient two-dimensional heat conduction analysis of isotropic FGM. The accuracy and efficiency of this method will be assessed. The paper is organized as follows.

In Sect. 2, the governing equation and integral form of thermal conduction in an isotropic non-homogeneous solid are described. The control volume finite element method for spatial discretization and the time-stepping scheme for time discretization of heat conduction equation are given in Sect. 3. To demonstrate the potential and accuracy of the method, examples are analyzed and the numerical results are compared with the results from analytical solutions or other well-published numerical solutions in Sect. 4. Finally, Sect. 5 provides a summary of the major results and presents relevant conclusions.

2 Governing equation

The transient heat conduction of an isotropic body which occupies a domain Ω is considered. We employ the rectangular Cartesian coordinates, x and y, to describe the temperature distribution inside the body. The thermal boundary conditions imposed upon the body are in the form of prescribed temperature $\hat{T}$ on the boundary Γ_θ, specified heat flux $\hat{q}$ on Γ_q and convective boundary condition on Γ_c. The union of the boundaries Γ_θ, Γ_q and Γ_c comprise Γ which is the whole boundary of the domain Ω.

In a functionally graded material, all material coefficients depend on the spatial coordinates. The material properties of an isotropic material are; thermal conductivity ($k = k(x, y)$), density ($\rho = \rho(x, y)$), and specific heat per unit mass ($c = c(x, y)$). The governing equation for transient two-dimensional heat conduction in isotropic and continuously non-homogenous solid is given by the following partial differential equation with variable coefficients

$$\frac{\partial}{\partial x}\left(k\frac{\partial T}{\partial x}\right) + \frac{\partial}{\partial y}\left(k\frac{\partial T}{\partial y}\right) + Q = \rho c\frac{\partial T}{\partial t}, \tag{1}$$

where $T = T(x, y, t)$ is the temperature field and $Q = Q(x, y, t)$ is the internal heat source per unit volume. The thermal conduction equation (1) has to be solved for prescribed boundary and initial conditions. The initial condition specifies the temperature distribution of the entire solid at time zero, that is

$$T(x,y,0) = \bar{T}_0(x,y), \tag{2}$$

where $\bar{T}_0(x,y)$ is defined as a constant value or a function of the spatial coordinates, x and y. General forms of heat conduction boundary conditions are

$$T = \hat{T} \quad \text{on } \Gamma_\theta, \tag{3a}$$

$$k\left(\frac{\partial T}{\partial x}n_x + \frac{\partial T}{\partial y}n_y\right) = \hat{q} \quad \text{on } \Gamma_q, \tag{3b}$$

$$k\left(\frac{\partial T}{\partial x}n_x + \frac{\partial T}{\partial y}n_y\right) + h(T - T_\infty) = 0 \quad \text{on } \Gamma_c, \tag{3c}$$

where $\hat{T}$ is the value of temperature at the boundary, h is the convection coefficient, T_∞ is the temperature of the surrounding medium, $\hat{q}$ is the normal heat flux that flow into or out of the domain, n_x and n_y are the components in x and y directions, respectively, of unit normal vector to the boundary Γ.

3 Control-volume finite element formulation

In this section, the weak formulation is first derived. Then, the control volume finite element method is applied to discretize the resulting integral equation from the previous step in both space and time. The discretized equation for each nodal unknown temperature can be assembled into matrices and vectors of all nodal temperatures. After applying the appropriate boundary conditions and initial condition, this system of linear algebraic equations is ready to be solved by a standard numerical technique.

3.1 Weak formulation

Firstly, Eq. 1 is integrated over a control volume Ω^{cv} and a time interval from t to $t + \Delta t$. Thus, integration of Eq. 1 leads to

$$\int_t^{t+\Delta t}\int_{\Omega^{cv}} \frac{\partial}{\partial x}\left(k\frac{\partial T}{\partial x}\right)d\Omega dt + \int_t^{t+\Delta t}\int_{\Omega^{cv}} \frac{\partial}{\partial y}\left(k\frac{\partial T}{\partial y}\right)d\Omega dt + \int_t^{t+\Delta t}\int_{\Omega^{cv}} Qd\Omega\, dt - \int_t^{t+\Delta t}\int_{\Omega^{cv}} \rho c\frac{\partial T}{\partial t}d\Omega\, dt = 0. \tag{4}$$

Applying the divergence theorem to the first two term on the left-handed side of Eq. 4 results in

$$\int_t^{t+\Delta t}\int_{\Gamma^{cs}} k\left(\frac{\partial T}{\partial x}n_x + \frac{\partial T}{\partial y}n_y\right)d\Gamma dt + \int_t^{t+\Delta t}\int_{\Omega^{cv}} Qd\Omega\, dt - \int_t^{t+\Delta t}\int_{\Omega^{cv}} \rho c\frac{\partial T}{\partial t}d\Omega\, dt = 0. \tag{5}$$

After imposing the heat flux and heat convection boundary conditions on the left-handed side of Eq. 5, it becomes

$$\int_t^{t+\Delta t}\int_{\Gamma_{int}} k\left(\frac{\partial T}{\partial x}n_x + \frac{\partial T}{\partial y}n_y\right)d\Gamma dt - \int_t^{t+\Delta t}\int_{\Gamma_q} \hat{q}d\Gamma\, dt - \int_t^{t+\Delta t}\int_{\Gamma_c} h(T - T_\infty)d\Gamma\, dt + \int_t^{t+\Delta t}\int_{\Omega^{cv}} Qd\Omega\, dt - \int_t^{t+\Delta t}\int_{\Omega^{cv}} \rho c\frac{\partial T}{\partial t}d\Omega\, dt = 0. \tag{6}$$

where Γ_{int} denotes an internal boundary of computational domain which is the sum of control surfaces from the surrounding elements contributing to a control volume formation.

3.2 Control volume finite element method

In view of the spatial discretization, the control volume is a union of sub-control volumes inside the three-node linear triangular elements or six-node quadratic triangular elements. For instance, a sub-control volume surrounding node I is constructed by connecting midpoints of the element edges I–J and I–K to the centroid of the element named I–J–K as shown in Fig. 1a. Figure 1b illustrates six sub-control volumes within a quadratic triangular element. The formation of a control volume for quadratic triangular

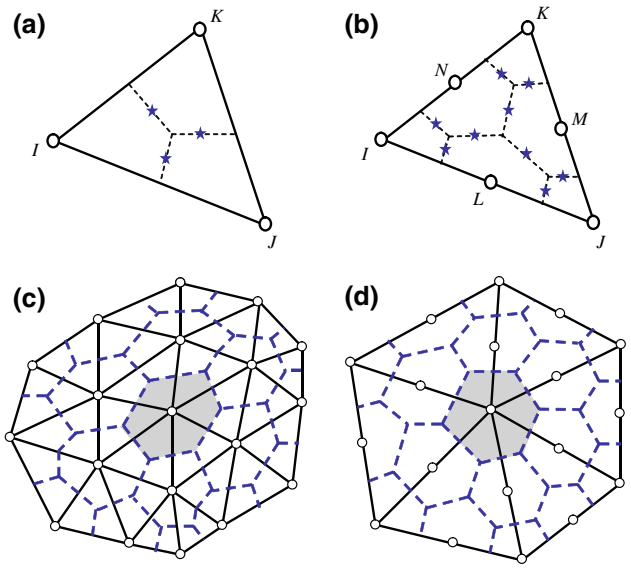

Fig. 1 The sub-control volume and its integration points of a control volume around each node in general **a** three-node triangular element, **b** six-node triangular element; typical shapes of control-volumes for a group of **c** three-node triangular elements, **d** six-node triangular elements

element is, in fact, the formation of sub-control volumes of four smaller "imitation" triangles *I–L–N*, *J–M–L*, *L–M–N*, and *K–N–M*. Figure 1c, d show two control volumes constructed from three-node and six-node triangular elements, respectively.

According to the concept of multiple isoparametric transformation proposed by Li et al. [29], the material properties and temperature at any point in a triangular element can be approximated by

$$\rho=\sum_{i=1}^{n}N_i\rho_i,\ c=\sum_{i=1}^{n}N_ic_i,\ k=\sum_{i=1}^{n}N_ik_i,\ T=\sum_{i=1}^{n}N_iT_i. \tag{7}$$

Here, N_i are the shape functions of the element [34] which are normally defined in terms of local coordinates over the triangular region, n is a number of nodes in a particular element, ρ_i, c_i, k_i, and T_i are the nodal values of density, specific heat, thermal conductivity, and temperature, respectively, of a particular element. Note that Eq. 7 is similar to the generalized isoparametric graded finite elements of Kim and Paulino [30]. The temperature gradients at any point in an element, appearing in the first integral of Eq. 5, can be written as

$$\frac{\partial T}{\partial x}=\sum_{i=1}^{n}\frac{\partial N_i}{\partial x}T_i, \tag{8a}$$

$$\frac{\partial T}{\partial y}=\sum_{i=1}^{n}\frac{\partial N_i}{\partial y}T_i, \tag{8b}$$

where $\frac{\partial N_i}{\partial x}$ and $\frac{\partial N_i}{\partial y}$ are the derivatives of shape functions at the nodal point i with respect to x and y, respectively. The midpoint rule is utilized to compute all element integrals since it gives high accuracy with little effort expended. The star symbols in Fig. 1a, b represent the integration points for determining the values of integral terms in Eq. 6. Note that the sub-control volume boundary around each node is the summation of two surfaces in the case of three-node element while it is the summation of four surfaces in the case of six-node element. Details of shape functions, their derivatives and numerical integration method are included in Appendix 1.

3.3 Time discretization

Integration with respect to time can be carried out with the following trapezoidal interpolation formula [13]:

$$\int_t^{t+\Delta t}\phi dt=\left[f\phi^{t+\Delta t}+(1-f)\phi^t\right]\Delta t, \tag{9}$$

where f is a weighting factor between 0 and 1. In this paper, the time discretization is done through a fully implicit scheme, $f=1$. Thus, the integrals of Eq. 6 can be written in discretized forms as

$$\int_t^{t+\Delta t}\int_{\Gamma_{\text{int}}}k\left(\frac{\partial T}{\partial x}n_x+\frac{\partial T}{\partial y}n_y\right)d\Gamma dt =\sum_{j=1}^{ng}\left[k\delta S^{\text{int}}\left(\frac{\partial T}{\partial x}n_x+\frac{\partial T}{\partial y}n_y\right)\right]_j\Delta t, \tag{10a}$$

$$\int_t^{t+\Delta t}\int_{\Gamma_q}\hat{q}d\Gamma dt=\sum_{i=1}^{nf}[\hat{q}_i\delta S_i^q]\Delta t, \tag{10b}$$

$$\int_t^{t+\Delta t}\int_{\Gamma_c}h(T-T_\infty)d\Gamma dt=\sum_{i=1}^{nc}\left[h_i\delta S_i^c\left(T_i^n-(T_\infty)_i^n\right)\right]\Delta t, \tag{10c}$$

$$\int_t^{t+\Delta t}\int_{\Omega^{\text{cv}}}Qd\Omega\,dt=\left(\int_{\Omega^{\text{cv}}}Qd\Omega\right)\Delta t, \tag{10d}$$

$$\int_t^{t+\Delta t}\int_{\Omega^{\text{cv}}}\rho c\frac{\partial T}{\partial t}d\Omega\,dt=\left(T_i^n-T_i^{n-1}\right)\left(\int_{\Omega^{\text{cv}}}\rho cd\Omega\right), \tag{10e}$$

where ng, nf, and nc are the number of surface segments belonging to Γ_{int}, Γ_q and Γ_c, respectively. δS^{int} is an internal surface of sub-control volume. δS_i^c, and δS_i^q are the surfaces associated with heat convection, and the heat flux at boundary corresponding to node i, respectively. T_i^{n-1} is the known temperature at the last time step t^{n-1} of node i, T_i^n is the unknown temperature at current time step t^n of node i, $\left(\frac{\partial T}{\partial t}\right)^{n-1}=\left(\frac{T_i^n-T_i^{n-1}}{\Delta t}\right)$ and $\Delta t=t^n-t^{n-1}$ is the size of time step. A special case with assuming that there is a uniform internal heat generation rate per unit volume throughout the domain can be used to simplify Eq. 10d. The control-volume finite element approximation of heat equation can be obtained by substituting Eq. 10a through to Eq. 10e into Eq. 6,

$$[K]\{T^n\}=\{f\}. \tag{11}$$

The coefficient matrix $[K]$ depends on the temperature gradients and the material properties. The right-handed side vector $\{f\}$ depends on the temperature results from the previous time step, specified heat flux, internal heat generation rate and heat convection coefficient. The remaining task is solving the system of equations (Eq. 11) for the nodal values of unknown temperatures T^n at current time step by using direct or iterative method. If the final time step has not reached, the last nodal temperatures are used as the current nodal temperatures for the next time step.

4 Numerical results and discussion

4.1 Assessment on predictive quality of the proposed method

The example used here is the steady heat conduction in a rectangular plate made of homogeneous material with the size of 5 m × 10 m as shown in the Fig. 2. The thermal conductivity of material is 1 W/m °C. The boundary conditions are $T(x, 0) = 0, T(0, y) = 0, T(x, 10) = 100 \sin(\pi x/10)$, and $\partial T/\partial x = 0$ at $x = 5$. To assess the accuracy of linear and quadratic CVFEM and the effect of mesh refinement versus analytical solution, four meshes are introduced, see Fig. 3.

The governing equation for this example is

$$\frac{\partial^2 T}{\partial x^2} + \frac{\partial^2 T}{\partial y^2} = 0 \tag{12}$$

The exact temperature field is

$$T(x, y) = 100 \frac{\sinh(\pi y/10)\sin(\pi x/10)}{\sinh \pi} \tag{13}$$

The average error of temperature field is evaluated by

$$E(x, y) = \left[\frac{1}{\mathrm{NIxNJ}} \sum_{i=1}^{\mathrm{NIxNJ}} \left|\frac{T_{Num} - T_{Exact}}{T_{Exact}}\right|\right] \times 100\% \tag{14}$$

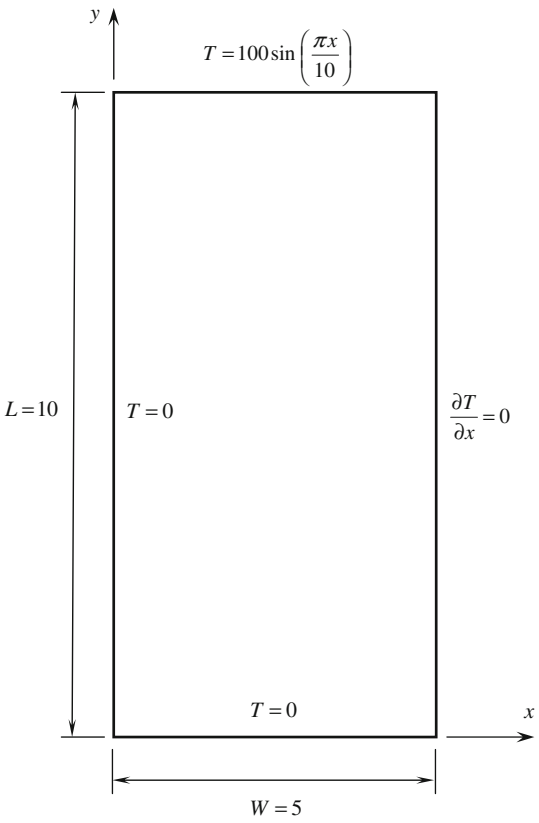

Fig. 2 The calculation domain and boundary conditions

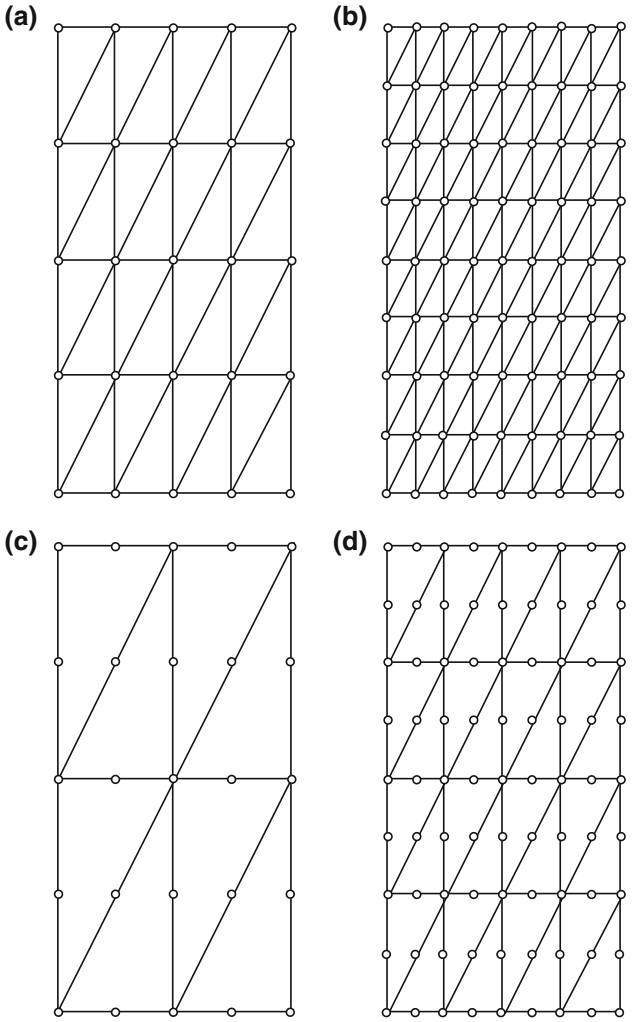

Fig. 3 The computational mesh of CVFEM **a** 25 nodes 32 elements (linear), **b** 81 nodes 128 elements (linear), **c** 25 nodes 8 elements (quadratic), **d** 81 nodes 32 elements (quadratic)

where T_{Num} and T_{Exact} are the numerical and exact values of temperature, respectively. NI and NJ are total numbers of internal nodes in x and y directions, respectively. From Table 1, the accuracy of numerical solution can be greatly improved by increasing the order of interpolation function just the same way as decreasing the element size, see Table 2.

4.2 Problems on FGM material

In this section, four simple heat conduction problems in isotropic FGM are presented in order to validate and illustrate the accuracy of the proposed numerical scheme. In all problems, zero initial temperature is applied.

The first test case is about solving the transient temperature for one-dimensional heat conduction problem. A functionally graded finite square strip with a unidirectional variation of thermal conductivity and thermal

Table 1 Average errors of various mesh sizes and orders of interpolation functions

CVFEM	Order	NI	NJ	$E(x, y)$ (%)
Mesh (a)	1	4	3	4.235
Mesh (b)	1	8	7	1.003
Mesh (c)	2	4	3	1.074
Mesh (d)	2	8	7	0.099

diffusivity [9] is concerned. The geometry, boundary conditions and mesh are given in Fig. 4. The thermal conductivity and diffusivity are assumed in the form of exponential functions, given by

$$k = k_0 e^{\lambda x}, \tag{15a}$$

$$\alpha = \frac{k}{\rho c} = \alpha_0 e^{\lambda x}, \tag{15b}$$

where $k_0 = 17$ W/(m °C), and $\alpha_0 = 0.17 \times 10^{-4}\text{m}^2/\text{s}$.

Three values of exponential parameters $\lambda = 0$, 0.2, and 0.5 cm^{-1} are used in this problem to demonstrate the non-homogeneous effect of material properties on the temperature result. In the view of boundary conditions, there is no normal heat flux on two opposite sides parallel to the y-axis while different values of temperature are specified on the two opposite sides parallel to the x-axis. The length of square strip is $a = 0.04$ m. The left boundary is maintained at zero temperature and the right boundary is imposed by the Heaviside step function of time, i.e., $T = \bar{T} \cdot H(t)$ with $\bar{T} = 1$ °C. The analytical solution of the temperature distribution in a FGM square strip at steady state can be obtained as

$$T = \bar{T}\left[\frac{e^{-\lambda x} - 1}{e^{-\lambda a} - 1}\right]. \tag{16}$$

When the exponential parameter is prescribed to zero, the strip has homogeneous thermal conductivity, $k = k_0$ and constant thermal diffusivity, $\alpha = \alpha_0$. The analytical solution for this special case [31] can be written as

$$T = \bar{T}\frac{x}{a} + \frac{2}{\pi}\sum_{n=1}^{\infty}\left[\frac{\bar{T}\cos(n\pi)}{n}\sin\frac{n\pi x}{a}\right]\text{e}^{\left(-\frac{n^2\pi^2 t}{a^2}\right)}. \tag{17}$$

The accuracy of this proposed method is evaluated by comparing the numerical results with the analytical solution in Eq. 17. All of the results are obtained by using 25 nodes, 4 quadratic triangular elements, and uniform time step $\Delta t = 1$ s.

Figure 5 shows the temperature change with time which is numerically and analytically computed at three positions, $x = 0.01$ m, $x = 0.02$ m, and $x = 0.03$ m. Good agreement between the numerical and analytical solutions is noticed in Fig. 5. Figure 6 shows the variation of temperature with time for three λ-values at the position $x = 0.02$ m. The temperature distribution in material having large exponent coefficient approaches the steady state solution quicker than that in the material having small exponent coefficient. Figure 7 illustrates the distributions of temperatures inside FGM strip under different transient states. From numerical results, it is found that the temperature approaches steady state after $t = 20$ s.

For the steady state condition, the analytical results from Eq. 16 are compared with the results obtained by the proposed method in Fig. 8. The numerical results are in good agreement with the analytical results. The predictive quality of CVFEM is also compared with conventional finite element method where the thermal conductivity of material is piecewise constant and represented by the value at the centroid of the element. The result suggests that the conventional FEM is not recommended for the solution of highly graded material especially in conjunction with coarse mesh, see Table 3.

In the second problem, a thick-wall functionally graded cylinder with infinite length is considered, where its inner radii R_1 is 0.08 m and outer radii R_2 is 0.1 m. The zero initial temperature is employed in this analysis. The outer surface of the hollow cylinder has the Heaviside step time variation $T = \bar{T} \cdot H(t)$ with $\bar{T} = 1$ °C. The inner surface is maintained at zero temperature. Due to symmetry in geometry and boundary conditions, only a quarter of annulus cross-section is considered. The total number of nodes and elements are 63 and 16, respectively. A uniform time step $\Delta t = 1.0$ s is used in this calculation. The geometry, boundary conditions and mesh for the second

Table 2 Comparison between exact and numerical solutions inside the calculation domain at corresponding locations

y	x	Exact solution, T_{exact}	CVFEM (3 node), Mesh (a)		CVFEM (6 node), Mesh (c)	
			T_{FVM3}	Error (%)	T_{FVM6}	Error (%)
2.5	2.5	5.319	5.6386	6.0086	5.351	0.6016
	5	7.522	7.9742	6.0117	7.601	1.0503
5	2.5	14.09	14.7109	4.4067	13.832	1.8311
	5	19.927	20.8043	4.4026	19.831	0.4818
7.5	2.5	32.01	32.7416	2.2855	32.454	1.3871
	5	45.269	46.3036	2.2854	45.93	1.4602

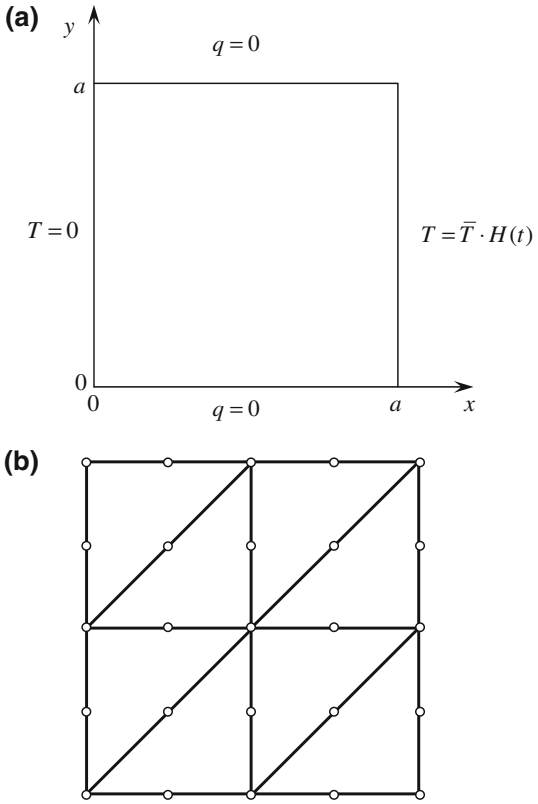

Fig. 4 **a** Geometry and boundary conditions of the functionally graded finite square strip problem, **b** triangular mesh

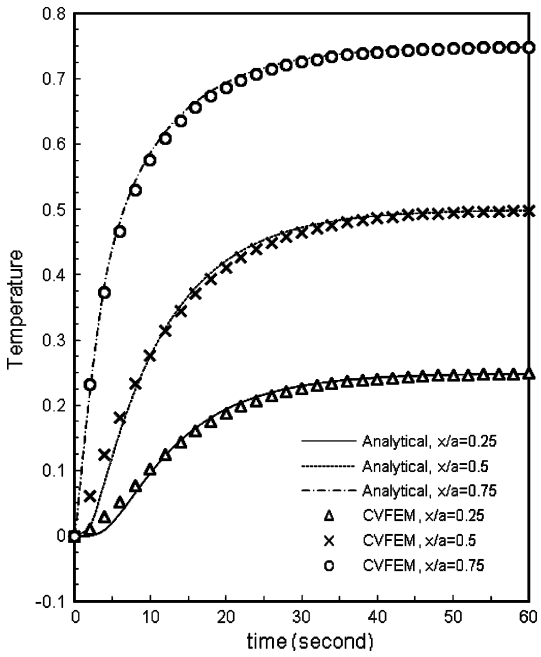

Fig. 5 CVFEM and analytical solutions for time dependence of temperature in a homogeneous finite square strip ($\lambda = 0$) at three locations along x-axis

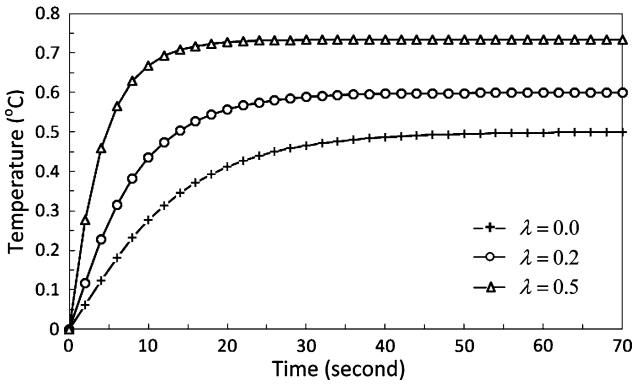

Fig. 6 Time dependence of temperature at the middle location of functionally graded finite square strip

problem are depicted in Fig. 9. The thermal conductivity and diffusivity are assumed in the form of exponential functions, given by

$$k = k_0 e^{\lambda(r-R_1)}, \tag{18a}$$

$$\alpha = \frac{k}{\rho c} = \alpha_0 e^{\lambda(r-R_1)}, \tag{18b}$$

where $k_0 = 17$ W/(m °C), $\alpha_0 = 0.17 \times 10^{-4}$ m^2/s. λ is a parameter dictating the non-homogeneity within the FGM cylinder. The analytical solution for homogeneous cylinder is given by [31] as follow

$$T(r,t) = \frac{\ln(r/R_1)}{\ln(R_2/R_1)} - \pi \sum_{n=1}^{\infty} \frac{J_0^2(R_1\zeta_n)U_0(r\zeta_n)}{J_0^2(R_1\zeta_n) - J_0^2(R_2\zeta_n)} e^{\left(-\alpha\zeta_n^2 t\right)}, \tag{19}$$

where

$$U_0(r\zeta_n) = J_0(r\zeta_n)Y_0(R_2\zeta_n) - J_0(R_2\zeta_n)Y_0(r\zeta_n), \tag{20}$$

and ζ_n are roots of the following transcendental equation

$$J_0(R_1 r)Y_0(R_2 r) - J_0(R_2 r)Y_0(R_1 r) = 0, \tag{21}$$

with $J_0(x)$ and $Y_0(x)$ are the zeroth order Bessel functions of first and second kind.

Some small differences between analytical and numerical solutions are observable in Fig. 10. Figure 11 shows the temperature profiles along the radial locations of homogeneous hollow cylinder at four different time instants. Numerical results for the time variation of temperature at $r = 9$ cm are illustrated in Fig. 12. Figure 13 gives the temperature profiles along the radial coordinate with various values of λ.

To illustrate the accuracy of the program in response to convective boundary, a rectangular FGM strip subjected to a non-uniform convective boundary condition in Fig. 14 is selected. The initial temperature of the plate is zero. The values of fluid temperature surrounding the bottom and the top edge of the plate are defined by function $T_d f_a(x)$ and

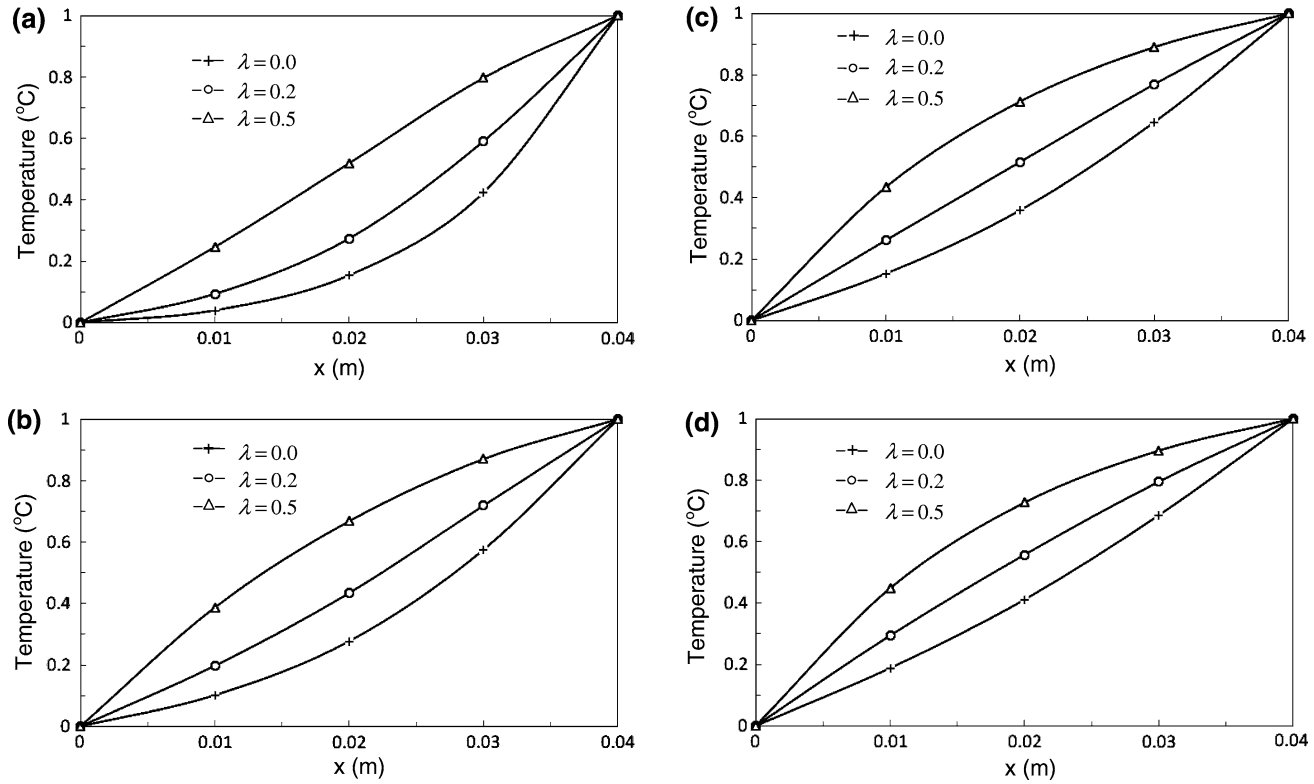

Fig. 7 Temperature distribution along x-axis of functionally graded finite square strip at **a** $t = 5$ s, **b** $t = 10$ s, **c** $t = 15$ s and **d** $t = 20$ s

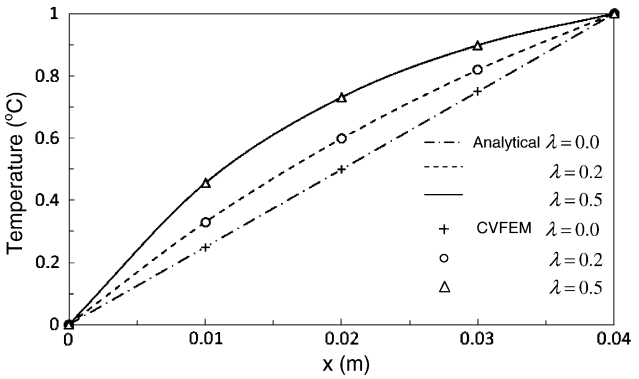

Fig. 8 Comparison of CVFEM and analytical solutions for steady temperature distribution along x-axis of functionally graded finite square strip

zero, respectively. The left and right boundaries are specified with zero normal temperature gradient. The non-dimensional parameters used in the third and fourth problems are defined as follow:

$$\bar{x} = x/B, \quad \bar{L} = L/B, \quad \tau = \alpha_o t/B^2, \quad \alpha_0 = k_0/(\rho c),$$
$$H_a = h_a/k_a, \quad H_b = h_b/k_b, \tag{22}$$

where τ represents the non-dimensional time and α_0 is a typical value of thermal diffusivity. The assigned values for non-dimensional parameters are given by

Table 3 Comparison on predictive quality between conventional FEM and CVFEM

λ	x	Exact	FEM (6 node)		CVFEM (6 node)	
			T_{FEM}	Error (%)	T_{CVFEM}	Error (%)
0.2	0.01	0.329179	0.309017	6.12489	0.32932	0.043493
	0.02	0.598688	0.599746	0.17678	0.59868	0.000611
	0.03	0.819343	0.805994	1.62921	0.81944	0.011738
0.5	0.01	0.455054	0.394336	13.3431	0.45772	0.585373
	0.02	0.731059	0.733122	0.28225	0.73101	0.006371
	0.03	0.898464	0.87677	2.41453	0.89944	0.108555

$$H_a = 1, \quad H_b = 1, \quad T_a = 1, \quad T_b = 0, \quad L = 6,$$
$$B = 1, \quad k_0 = 1, \quad \alpha_0 = 1, \tag{23}$$

and a function $f_a(x)$ is defined by

$$f_a(\bar{x}) = \begin{cases} 1 - [\bar{x}'/\bar{x}_0]^2 & : -\bar{x}_0 \le \bar{x}' \le \bar{x}_0 \\ 0 & : \bar{x}' \le -\bar{x}_0,\ \bar{x}_0 \ge \bar{x}' \end{cases}. \tag{24}$$
$$\bar{x}_0 = 1,\ \bar{x}' = \bar{x} - L/2$$

The definition of function $f_b(x)$ is not necessary because the temperature of surrounding fluid on the top edge of a plate is prescribed to zero.

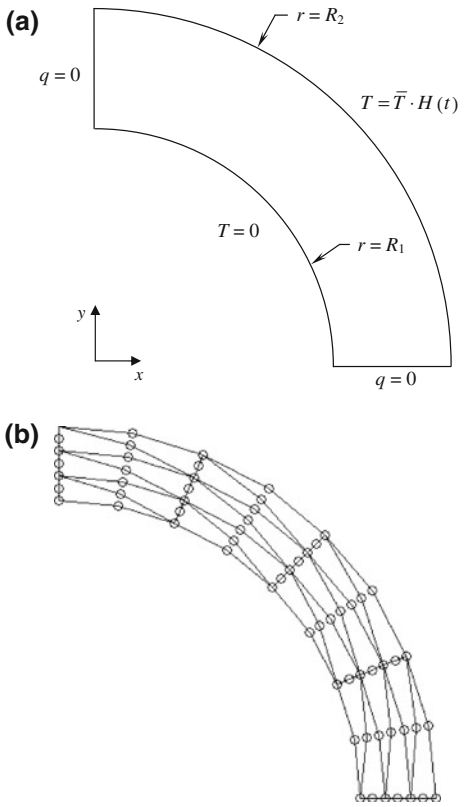

Fig. 9 **a** Geometry of the second problem and boundary conditions, **b** triangular mesh

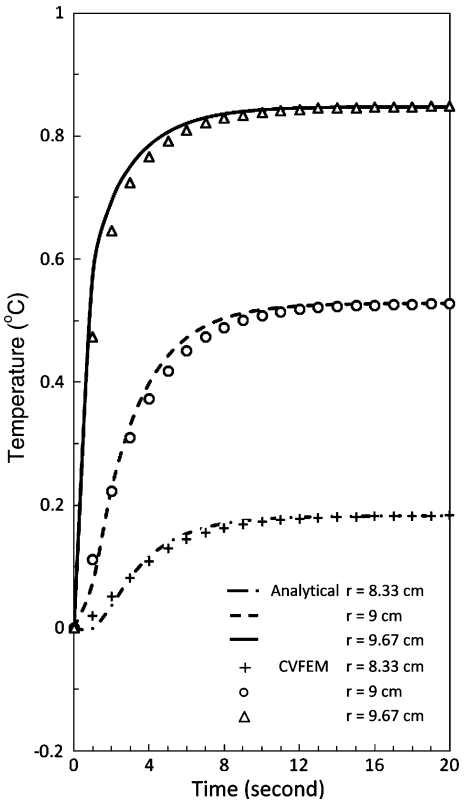

Fig. 10 Time dependence of temperature at three radial positions in a homogenous hollow cylinder

The thermal conductivity and diffusivity at any point in the FGM plate are assumed following the exponential functions as

$$k = k_0 e^{\lambda y/B} \tag{25a}$$

$$\alpha = \frac{k}{\rho c} = \alpha_0 e^{\lambda y/B} \tag{25b}$$

where λ represents the non-homogeneity parameter for controlling the material gradation through the thickness of the plate. In this problem, the number of equally spaced nodes along the x and y directions are 49 and 11, respectively. Initial temperature of the plate is zero and the time step is 0.01.

Figures 15 and 16 show the plot of temperature variation at the middle of the plate $(\bar{x} = 3)$ when $\tau = 0.1$ and $\tau = 10$. For the purpose of comparison, the analytical results of Ootao and Tanigawa [32] are also shown in both figures. It is notable that the steady state is reached after $\tau = 4$. Good agreement between the analytical and proposed numerical solutions can be seen.

The corresponding temperature distributions on the bottom edge of the rectangular plate with different λ-values and at different time instants are depicted in Fig. 17. The high temperature zone can be noticed in the heated region

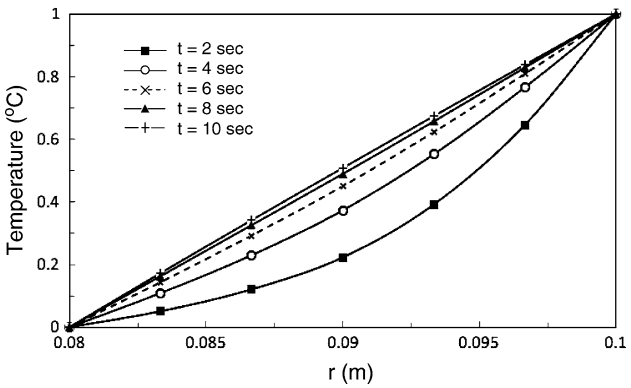

Fig. 11 Temperature variation with the radial distance at five time levels for a homogeneous hollow cylinder

near the midpoint on the bottom edge of the plate. When the parameter λ is decreased, the temperature value on the heated surface increases. Although this non-homogeneity effect can be clearly noticed at steady state, the temperature distributions of different λ-values in transient state are almost the same.

Finally, the third problem is considered again by assuming that the surrounding temperature on the bottom edge of the plate increased exponentially with time; viz.,

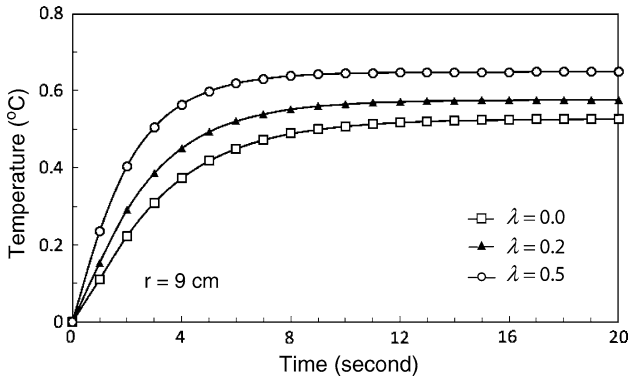

Fig. 12 Temperature variation with respect to time at $r = 9$ cm in a functionally graded hollow cylinder

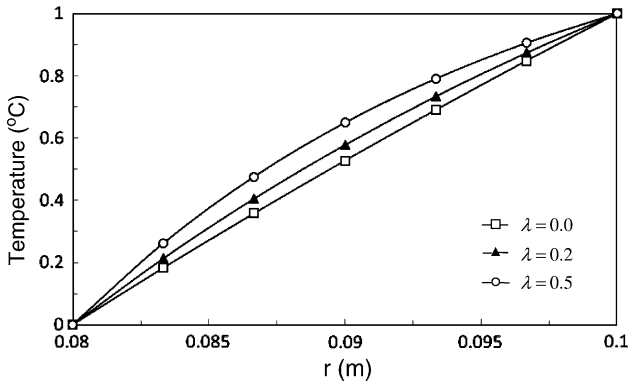

Fig. 13 Steady state temperature distribution with radial direction for a functionally graded hollow cylinder

$T_a f_a(x) g(\tau)$, where $g(\tau) = 1 - e^{-\gamma\tau}$. From this definition, γ is a parameter dictating the rate of change in fluid temperature imposed on the bottom edge of the plate. If γ is large, the value of function $g(\tau)$ increases abruptly like a unit step function. Figure 18 plots the time histories of temperature at the centroid of the plate for different values

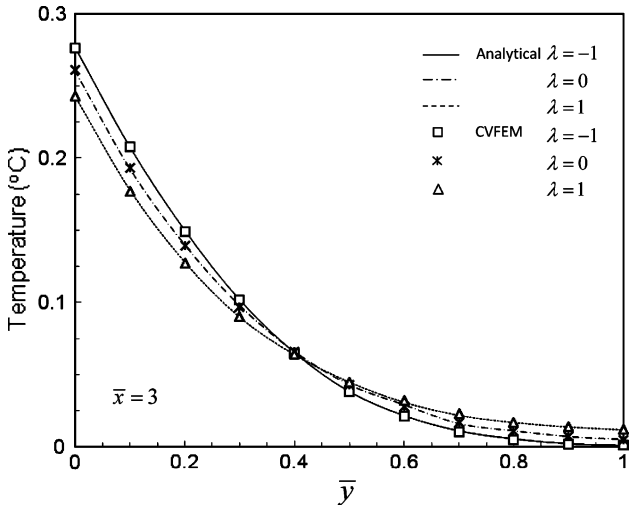

Fig. 15 Temperature change along the y-direction at the position $\bar{x} = 3$ when $\tau = 0.1$

of γ, with $\lambda = 1$. The results calculated from the present method match well with the results obtained from the meshless local Petrov–Galerkin (MLPG) method [33]. The effect of γ on temperature distributions throughout the thickness of the FGM plate with $\lambda = 1$ in a transient state ($\tau = 1$) at the position $\bar{x} = 3$ is shown in Fig. 19.

5 Summary and conclusions

The high order control-volume finite element method has been applied to analyze the transient heat conduction problems occurring in two-dimensional functionally graded solid. The material properties such as thermal conductivity, density, specific heat capacity and thermal diffusivity were assumed to vary exponentially through the thickness direction. In our validation work on homogeneous material,

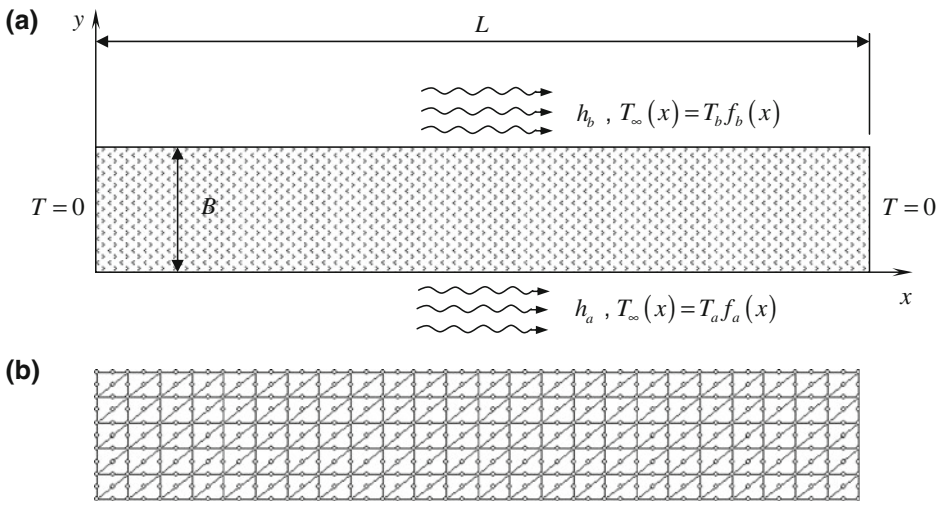

Fig. 14 **a** Geometry of the FGM plate subjected to non-uniform convection boundary conditions, **b** triangular mesh

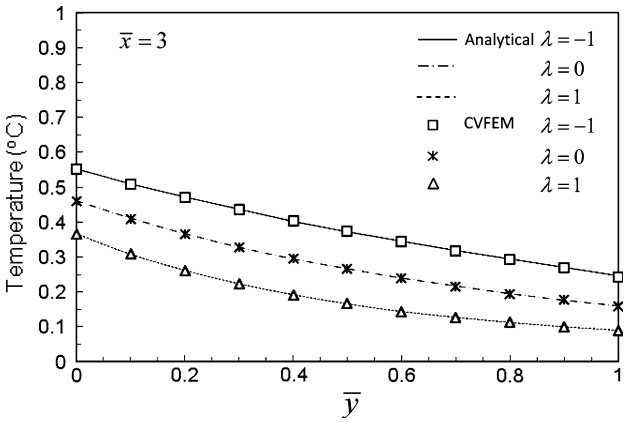

Fig. 16 Steady state temperature change along the y-direction at the position $\bar{x}=3$

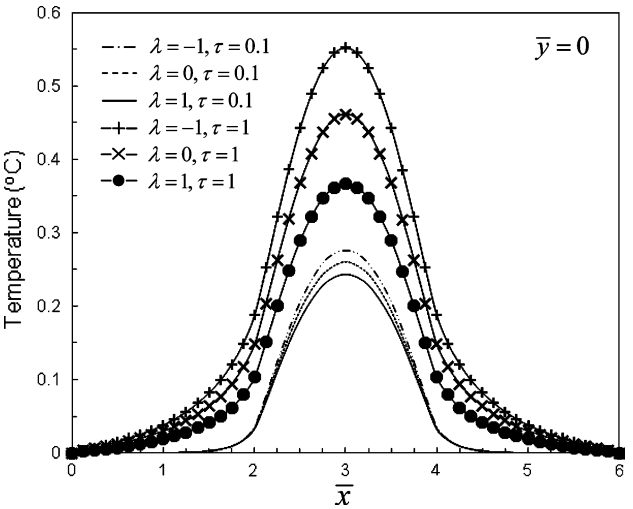

Fig. 17 Temperature distributions at different time instants on the bottom edge of the plate $(\bar{y}=0)$

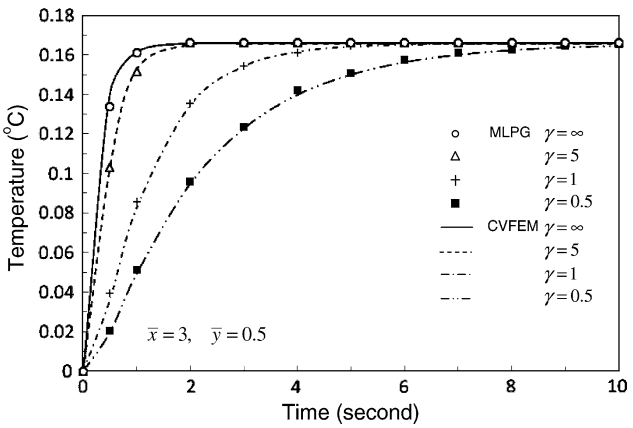

Fig. 18 Time history of temperature at the centroid of the plate for the time-dependent heat supply with $\lambda=1$

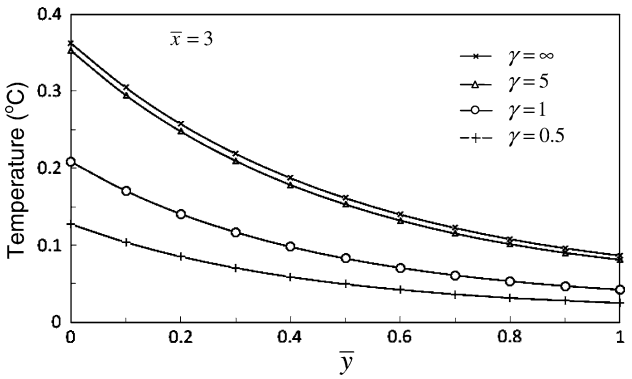

Fig. 19 Temperature distribution throughout the thickness of the rectangular FGM plate for the time-dependent heat supply at time $\tau=1$ and $\lambda=1$

it has been proven that this method gave better accuracy than the first order method under the same mesh size.

Later, the predictive quality of high-order CVFEM versus conventional high-order FEM was investigated by assessing the effect of non-homogeneity of the material properties on thermal response against the analytical result under the same mesh size. The result showed that our method could provide more accurate solution than the counterpart.

The solution with time-dependent boundary condition is also illustrated to show the flexibility of numerical method in solving the problems of interest. The transient temperature solutions of material obtained from the CVFEM method agree well with the solutions from MLPG methods. Our method could also perform well with the solution of heat transfer through a hollow cylinder. It is also recommended for solution of heat transfer with steady and unsteady convective boundary conditions.

The present formulation to be used for analyzing FGMs which their properties described by other grading functions is subjected to further investigation.

Acknowledgments The authors would like to acknowledge the financial support from National Metal and Materials Technology Center (MTEC), Thailand Science Park, under the research grant no.MT-B-52-MAC-22-189-G.

Appendix 1

Shape functions, their derivatives and numerical integration method

The shape functions and their derivatives with respect to ξ and η for 3-noded triangular element are summarized in Table 4. Figure 20 shows the mapping from arbitrary 3-node triangular element to a reference triangular element. The shape functions and their derivatives with respect to ξ

Table 4 The shape functions and their derivatives with respect to ξ and η for 3-noded triangular element

i	N_i	$\frac{\partial N_i}{\partial \xi}$	$\frac{\partial N_i}{\partial \eta}$
1	$1-\xi-\eta$	-1	-1
2	ξ	1	0
3	η	0	1

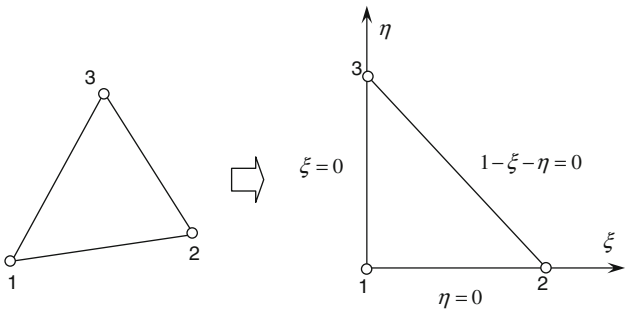

Fig. 20 Mapping from general triangle to a reference triangle (3 node element)

Table 5 The shape functions and their derivatives with respect to ξ and η for 6-noded triangular element

i	N_i	$\frac{\partial N_i}{\partial \xi}$	$\frac{\partial N_i}{\partial \eta}$
1	$(1-\xi-\eta)$ $(1-2\xi-2\eta)$	$-3+4\xi+4\eta$	$-3+4\xi+4\eta$
2	$\xi(2\xi-1)$	$4\xi-1$	0
3	$\eta(2\eta-1)$	0	$4\eta-1$
4	$4\xi(1-\xi-\eta)$	$4-8\xi-4\eta$	-4ξ
5	$4\xi\eta$	4η	4ξ
6	$4\eta(1-\xi-\eta)$	-4η	$4-4\xi-8\eta$

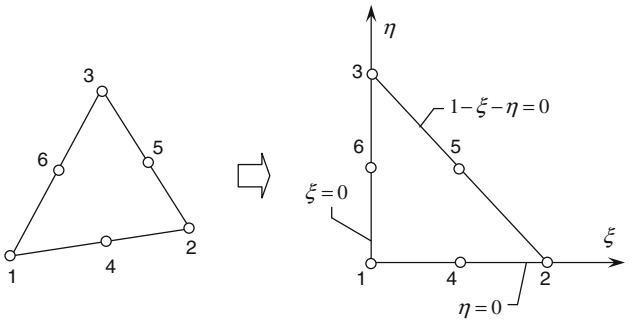

Fig. 21 Mapping from general triangle to a reference triangle (6 node element)

and η for 6-noded triangular element are summarized in Table 5. Figure 21 shows the mapping of element of arbitrary 6-node triangular element to a reference triangular element.

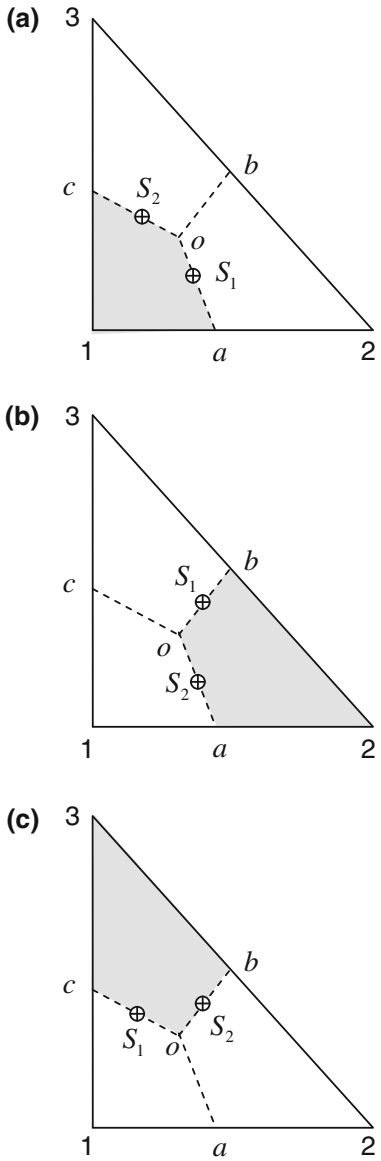

Fig. 22 Integration points along the faces surrounding **a** node 1, **b** node 2, **c** node 3

Table 6 Integration points for 3-node element (midpoint rule)

Face\node	1	2	3
S_1	(5/12,1/6)	(5/12,5/12)	(1/6,5/12)
S_2	(1/6,5/12)	(5/12,1/6)	(5/12,5/12)

In the derivation of the element conductance matrix, it is necessary to establish the shape function derivatives with respect to (x, y) coordinates. By the rule of partial differentiation, we write the derivatives of the shape functions with respect to local coordinates as

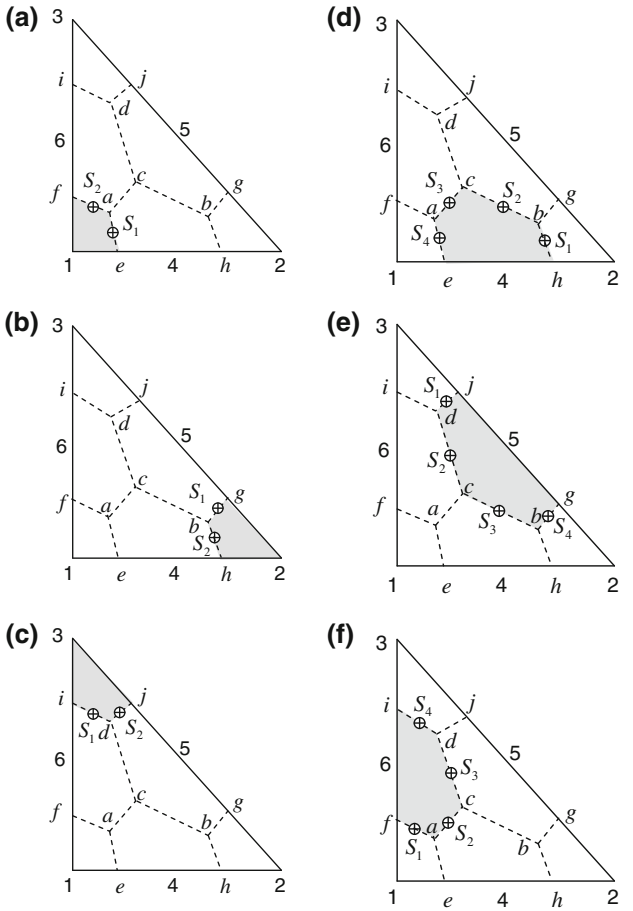

Fig. 23 Integration points along the faces surrounding **a** node 1, **b** node 2, **c** node 3, **d** node 4, **e** node 5, **f** node 6

$$\frac{\partial N_i}{\partial \xi} = \frac{\partial N_i}{\partial x}\frac{\partial x}{\partial \xi} + \frac{\partial N_i}{\partial y}\frac{\partial y}{\partial \xi} \tag{26}$$

$$\frac{\partial N_i}{\partial \eta} = \frac{\partial N_i}{\partial x}\frac{\partial x}{\partial \eta} + \frac{\partial N_i}{\partial y}\frac{\partial y}{\partial \eta} \tag{27}$$

in the algebraic form, or

$$\begin{Bmatrix} \frac{\partial N_i}{\partial \xi} \\ \frac{\partial N_i}{\partial \eta} \end{Bmatrix} = \begin{bmatrix} \frac{\partial x}{\partial \xi} & \frac{\partial y}{\partial \xi} \\ \frac{\partial x}{\partial \eta} & \frac{\partial y}{\partial \eta} \end{bmatrix} \begin{Bmatrix} \frac{\partial N_i}{\partial x} \\ \frac{\partial N_i}{\partial y} \end{Bmatrix} = [J] \begin{Bmatrix} \frac{\partial N_i}{\partial x} \\ \frac{\partial N_i}{\partial y} \end{Bmatrix} \tag{28}$$

in the matrix form. The matrix $[J]$ is known as the Jacobian matrix. The Jacobian matrix components can be found explicitly in terms of the local coordinates as follows,

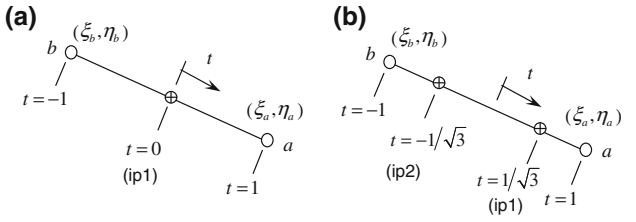

Fig. 24 **a** Integration point for midpoint rule. **b** Integration points for 2-point Gauss-Quadrature rule

$$\frac{\partial x}{\partial \xi} = \sum_{i=1}^{\text{npe}} \frac{\partial N_i}{\partial \xi} x_i, \quad \frac{\partial y}{\partial \xi} = \sum_{i=1}^{\text{npe}} \frac{\partial N_i}{\partial \xi} y_i,$$
$$\frac{\partial x}{\partial \eta} = \sum_{i=1}^{\text{npe}} \frac{\partial N_i}{\partial \eta} x_i, \frac{\partial y}{\partial \eta} = \sum_{i=1}^{\text{npe}} \frac{\partial N_i}{\partial \eta} y_i, \tag{29}$$

where npe refers to the number of nodes per element.

Therefore, the required derivatives $\frac{\partial N_i}{\partial x}$ and $\frac{\partial N_i}{\partial y}$ can be obtained by

$$\begin{Bmatrix} \frac{\partial N_i}{\partial x} \\ \frac{\partial N_i}{\partial y} \end{Bmatrix} = [J]^{-1} \begin{Bmatrix} \frac{\partial N_i}{\partial \xi} \\ \frac{\partial N_i}{\partial \eta} \end{Bmatrix} \tag{30}$$

The discretized equation for heat conduction at steady state of the control volume belonging to node i is

$$\sum_{k=1}^{\text{ns}} \left\{ \left(k\frac{\partial T}{\partial x}\right) n_x + \left(k\frac{\partial T}{\partial y}\right) n_y \right\}_k \Delta A_k + \bar{S}_I \Delta V_I = 0 \tag{31}$$

where ΔA_k represents the area of face k of the control volume covering node i; ns is the total number of faces; ΔV_I is the volume of the control volume belonging to node i; $\bar{S}_I$is the average heat source over the control volume; n_x and n_y are the direction cosines of a surface. For example, n_x and n_y of the face S_1 in Fig. 22a, later referred to as S_{oa}, are defined as

$$n_x = \frac{y_o - y_a}{\Delta A}, \quad n_y = \frac{x_a - x_o}{\Delta A}, \tag{32}$$

where $\Delta A = \sqrt{(x_o - x_a)^2 + (y_o - y_a)^2}$.

Equation 31 may be rewritten in matrix form for a triangular element that relates to node i as

$$[K]\{T^e\} = \{f\} \tag{33}$$

where $[K]$ is the element conductance matrix; $\{T^e\}$ is the vector containing nodal temperature values in the element; $\{f\}$ is the element load vector.

Table 7 Integration points for 6-node element (midpoint rule)

Face\node	1	2	3	4	5	6
S_1	(5/24,1/12)	(17/24,5/24)	(1/12,17/24)	(17/24,1/12)	(5/24,17/24)	(1/12,5/24)
S_2	(1/12,5/24)	(17/24,1/12)	(5/24,17/24)	(1/2,1/4)	(1/4,1/2)	(1/4,1/4)
S_3	–	–	–	(1/4,1/4)	(1/2,1/4)	(1/4,1/2)
S_4	–	–	–	(5/24,1/12)	(17/24,5/24)	(1/12,17/24)

Table 8 Integration points for 6-node element (2-point Gauss quadrature rule)

Face\node	1	2	3	4	5	6
S_1						
ip1	(0.23239,0.03522)	(0.73239,0.23239)	(0.03522,0.73239)	(0.73329,0.03522)	(0.23239,0.73239)	(0.03522,0.23239)
ip2	(0.18428,0.13145)	(0.68428,0.18428)	(0.13145,0.68428)	(0.68428,0.13145)	(0.18428,0.68428)	(0.13145,0.18428)
S_2						
ip1	(0.13145,0.18428)	(0.68428,0.13145)	(0.18428,0.68428)	(0.59623,0.20189)	(0.20189,0.59623)	(0.20189,0.20189)
ip2	(0.03522,0.23239)	(0.73239,0.03522)	(0.23239,0.73239)	(0.40377,0.29811)	(0.29811,0.40377)	(0.29811,0.29811)
S_3						
ip1	–	–	–	(0.29811,0.29811)	(0.40377,0.29811)	(0.29811,0.40377)
ip2	–	–	–	(0.20189,0.20189)	(0.59623,0.20189)	(0.20189,0.59623)
S_4						
ip1	–	–	–	(0.18428,0.13145)	(0.68428,0.18428)	(0.13145,0.68428)
ip2	–	–	–	(0.23239,0.03522)	(0.73239,0.23239)	(0.03522,0.73239)

The element conductance matrix and load vector

For brevity in the following expressions, the definition of $\Delta y_{mn} = y_m - y_n$ and $\Delta x_{mn} = x_m - x_n$ are introduced. Ω is defined as the area of an element.

3-node element:

The components of element conductance matrix and element load vector are

$$\begin{aligned}
K_{1,j} &= \left(k\frac{\partial N_j}{\partial x}\right)_{S_{oa}} \Delta y_{oa} - \left(k\frac{\partial N_j}{\partial y}\right)_{S_{oa}} \Delta x_{oa} + \left(k\frac{\partial N_j}{\partial x}\right)_{S_{co}} \\
&\quad \times \Delta y_{co} - \left(k\frac{\partial N_j}{\partial y}\right)_{S_{co}} \Delta x_{co}, \\
K_{2,j} &= \left(k\frac{\partial N_j}{\partial x}\right)_{S_{ob}} \Delta y_{ob} - \left(k\frac{\partial N_j}{\partial y}\right)_{S_{ob}} \Delta x_{ob} + \left(k\frac{\partial N_j}{\partial x}\right)_{S_{ao}} \\
&\quad \times \Delta y_{ao} - \left(k\frac{\partial N_j}{\partial y}\right)_{S_{ao}} \Delta x_{ao}, \\
K_{3,j} &= \left(k\frac{\partial N_j}{\partial x}\right)_{S_{oc}} \Delta y_{oc} - \left(k\frac{\partial N_j}{\partial y}\right)_{S_{oc}} \Delta x_{oc} + \left(k\frac{\partial N_j}{\partial x}\right)_{S_{bo}} \\
&\quad \times \Delta y_{bo} - \left(k\frac{\partial N_j}{\partial y}\right)_{S_{bo}} \Delta x_{bo}, \\
f_1 &= -\frac{\bar{S}_1\Omega}{3}, f_2 = -\frac{\bar{S}_2\Omega}{3}, f_3 = -\frac{\bar{S}_3\Omega}{3}.
\end{aligned} \tag{34}$$

6-node element:

The components of element conductance matrix and element load vector are

$$\begin{aligned}
K_{1,j} &= \left(k\frac{\partial N_j}{\partial x}\right)_{S_{ae}} \Delta y_{ae} - \left(k\frac{\partial N_j}{\partial y}\right)_{S_{ae}} \Delta x_{ae} + \left(k\frac{\partial N_j}{\partial x}\right)_{S_{fa}} \\
&\quad \times \Delta y_{fa} - \left(k\frac{\partial N_j}{\partial y}\right)_{S_{fa}} \Delta x_{fa}, \\
K_{2,j} &= \left(k\frac{\partial N_j}{\partial x}\right)_{S_{bg}} \Delta y_{bg} - \left(k\frac{\partial N_j}{\partial y}\right)_{S_{bg}} \Delta x_{bg} \\
&\quad + \left(k\frac{\partial N_j}{\partial x}\right)_{S_{hb}} \Delta y_{hb} - \left(k\frac{\partial N_j}{\partial y}\right)_{S_{hb}} \Delta x_{hb}, \\
K_{3,j} &= \left(k\frac{\partial N_j}{\partial x}\right)_{S_{id}} \Delta y_{id} - \left(k\frac{\partial N_j}{\partial y}\right)_{S_{id}} \Delta x_{id} + \left(k\frac{\partial N_j}{\partial x}\right)_{S_{dj}} \\
&\quad \times \Delta y_{dj} - \left(k\frac{\partial N_j}{\partial y}\right)_{S_{dj}} \Delta x_{dj}, \\
K_{4,j} &= \left(k\frac{\partial N_j}{\partial x}\right)_{S_{bh}} \Delta y_{bh} - \left(k\frac{\partial N_j}{\partial y}\right)_{S_{bh}} \Delta x_{bh} + \left(k\frac{\partial N_j}{\partial x}\right)_{S_{cb}} \\
&\quad \times \Delta y_{cb} - \left(k\frac{\partial N_j}{\partial y}\right)_{S_{cb}} \Delta x_{cb} \left(k\frac{\partial N_j}{\partial x}\right)_{S_{ac}} \Delta y_{ac} \\
&\quad - \left(k\frac{\partial N_j}{\partial y}\right)_{S_{ac}} \Delta x_{ac} + \left(k\frac{\partial N_j}{\partial x}\right)_{S_{ea}} \Delta y_{ea} \\
&\quad - \left(k\frac{\partial N_j}{\partial y}\right)_{S_{ea}} \Delta x_{ea}, \\
K_{5,j} &= \left(k\frac{\partial N_j}{\partial x}\right)_{S_{dj}} \Delta y_{dj} - \left(k\frac{\partial N_j}{\partial y}\right)_{S_{dj}} \Delta x_{dj} + \left(k\frac{\partial N_j}{\partial x}\right)_{S_{cd}} \Delta y_{cd} \\
&\quad - \left(k\frac{\partial N_j}{\partial y}\right)_{S_{cd}} \Delta x_{cd} \left(k\frac{\partial N_j}{\partial x}\right)_{S_{bc}} \Delta y_{bc} - \left(k\frac{\partial N_j}{\partial y}\right)_{S_{bc}} \Delta x_{bc} \\
&\quad + \left(k\frac{\partial N_j}{\partial x}\right)_{S_{gb}} \Delta y_{gb} - \left(k\frac{\partial N_j}{\partial y}\right)_{S_{gb}} \Delta x_{gb}, \\
K_{6,j} &= \left(k\frac{\partial N_j}{\partial x}\right)_{S_{af}} \Delta y_{af} - \left(k\frac{\partial N_j}{\partial y}\right)_{S_{af}} \Delta x_{af} + \left(k\frac{\partial N_j}{\partial x}\right)_{S_{ca}} \Delta y_{ca} \\
&\quad - \left(k\frac{\partial N_j}{\partial y}\right)_{S_{ca}} \Delta x_{ca} \left(k\frac{\partial N_j}{\partial x}\right)_{S_{dc}} \Delta y_{dc} - \left(k\frac{\partial N_j}{\partial y}\right)_{S_{dc}} \Delta x_{dc} \\
&\quad + \left(k\frac{\partial N_j}{\partial x}\right)_{S_{id}} \Delta y_{id} - \left(k\frac{\partial N_j}{\partial y}\right)_{S_{id}} \Delta x_{id}, \\
f_1 &= -\frac{\bar{S}_1\Omega}{12}, \quad f_2 = -\frac{\bar{S}_2\Omega}{12}, \quad f_3 = -\frac{\bar{S}_3\Omega}{12}, \quad f_4 = -\frac{\bar{S}_4\Omega}{4}, \\
f_5 &= -\frac{\bar{S}_5\Omega}{4}, \quad f_6 = -\frac{\bar{S}_6\Omega}{4}.
\end{aligned} \tag{35}$$

The calculation method for integrals of an element

The integration points on the faces surrounding node i for midpoint rule integration over the faces within a 3-noded triangular element are depicted in Fig. 22 and their locations are summarized in Table 6. The integration points of midpoint rule on the faces surrounding node i within a 6-noded triangular element are depicted in Fig. 23 and their locations are summarized in Table 7.

The surface integral can be calculated by the midpoint rule which its value equals to the product of the functional values at the center of surface and the total surface area. The locations of integration points are illustrated in Fig. 24.

The Gauss quadrature rule is used to approximate the integral value of a specified function. It is a sum of the products between the weighting factors and the corresponding function values at the gauss points. The integration points for mid-point rule and 2-point Gauss quadrature rule are calculated by

$$\begin{Bmatrix} \xi \\ \eta \end{Bmatrix} = \frac{1}{2}(1-t)\begin{Bmatrix} \xi_b \\ \eta_b \end{Bmatrix} + \frac{1}{2}(1+t)\begin{Bmatrix} \xi_a \\ \eta_a \end{Bmatrix}, \quad -1 \le t \le 1 \tag{36}$$

where

$t = 0$ for midpoint rule.
$t = \{+1/\sqrt{3}, -1/\sqrt{3}\}$ for 2-point Gauss quadrature rule.

The weighting factors for midpoint rule and 2-point Gauss quadrature rule are given by

$w_{ip1} = 2$ for midpoint rule.
$w_{ip1} = w_{ip2} = 1$ for 2-point Gauss quadrature rule.

The line integral of $F(S)$ over the finite length of ΔA can be simplified to

$\int_0^{\Delta A} F(S)dS \approx \left(\frac{\Delta A}{2}\right)(2)(f(0)) = f(0)\Delta A$ for midpoint rule,

$\int_0^{\Delta A} F(S)dS \approx \left(\frac{\Delta A}{2}\right)\left(f\left(+1/\sqrt{3}\right) + f\left(-1/\sqrt{3}\right)\right)$ for 2-point Gauss quadrature rule.

The integration points of 2-point Gauss quadrature rule on the faces surrounding node i within a 6-noded triangular element are summarized in Table 8.

References

1. Suresh S, Mortensen A (1997) Fundamentals of functionally graded materials. Cambridge University Press, Cambridge
2. Miyamoto Y, Kaysser WA, Rabin BH, Kawasaki A, Ford RG (1999) Functionally graded materials: design, processing and applications. Kluwer Academic, Dordrecht
3. Ni M, Leung MKH, Leung DYC (2007) Micro-scale modeling of solid oxide fuel cells with micro-structurally graded electrodes. J Power Sourc 168:369–378
4. Yang J, Xiang HJ (2007) A three-dimensional finite element study on the biomechanical behavior of an FGBM dental implant in surrounding bone. J Biomech 40:2377–2385
5. Jin ZH, Batra RC (1996) Stress intensity relaxation at the tip of an edge crack in a functionally graded material subjected to a thermal shock. J Therm Stresses 19:317–339
6. Noda N, Jin ZH (1994) A crack in functionally gradient materials under thermal shock. Arch Appl Mech 64:99–110
7. Jin ZH, Paulino GH (2001) Transient thermal stress analysis of an edge crack in a functionally graded material. Int J Fract 107:73–98
8. Sutradhar A, Paulino GH, Gray LJ (2002) Transient heat conduction in homogenous and non-homogeneous materials by the Laplace transform Galerkin boundary element method. Eng Anal Boundary Elem 26:119–132
9. Sladek J, Sladek V, Zhang Ch (2003) Transient heat conduction analysis in functionally graded materials by the meshless local boundary integral equation method. Comput Mater Sci 28:494–504
10. Wang BL, Mai YW, Zhang XH (2004) Thermal shock resistance of functionally graded materials. Acta Mater 52:4961–4972
11. Wang BL, Tian ZH (2005) Application of finite element-finite difference method to the determination of transient temperature field in functionally graded materials. Finite Elem Anal Des 41:335–349
12. Wang H, Qin QH, Kang YL (2006) A meshless model for transient heat conduction in functionally graded materials. Comput Mech 38:51–60
13. Verteeg HK, Malalasekera W (2007) An introduction to computational fluid dynamics: the finite volume method. Prentice-Hall, New York
14. Aboudi J, Pindera MJ, Arnold SM (1999) Higher-order theory for functionally graded materials. Composites Part B 33(8):777–832
15. Aboudi J, Pindera MJ, Arnold SM (2002) High-fidelity generalized method of cells for inelastic periodic multiphase materials. Paper no. NASA-TM-2002-211469
16. Bansal Y, Pindera MJ (2003) Efficient reformulation of the thermal higher-order theory for FGMs. J Therm Stresses 26(11/12):1055–1092
17. Bansal Y, Pindera MJ (2005) A second look at the higher-order theory for periodic multiphase materials. ASME J Appl Mech 72:177–195
18. Bansal Y (2005) Finite-Volume Direct Averaging Micromechanics of Heterogeneous Media. Ph.D. Thesis, Engineering and Applied Science University of Virginia, VA
19. Bansal Y, Pindera MJ (2006) Finite-volume direct averaging micromechanics of heterogeneous materials with elastic-plastic phases. Int J Plast 22(5):775–825
20. Pindera MJ, Bansal Y (2007) On the micromechanics-based simulation of metal matrix composite response. ASME J Eng Mater Technol 129:468–482
21. Cavalcante MAA (2006) Modeling of transient thermo-mechanical behavior of composite material structures by the finite-volume theory. M.S. Thesis, Civil Engineering Department, Federal University of Alagoas, Maceio
22. Cavalcante MAA, Marques SPC, Pindera MJ (2007) Parametric formulation of the finite-volume theory for functionally graded materials. Part I: analysis. ASME J Appl Mech 74(5):935–945
23. Cavalcante MAA, Marques SPC, Pindera MJ (2007) Parametric formulation of the finite-volume theory for functionally graded materials. Part II: numerical results. ASME J Appl Mech 74(5):946–957
24. Gao X, Song Y, Sun Z (2009) Quadrilateral subcell based finite volume micromechanics theory for multiscale analysis of elastic periodic materials. ASME J Appl Mech 76:011013-1–011013-7

25. Ferziger JH, Peric M (1996) Computational methods for fluid dynamics. Springer, New York
26. Prakash C, Patankar SV (1985) A control volume-based finite element method for solving the Navier-Stokes equations using equal-order velocity-pressure interpolation. Numer Heat Transfer 8:259–280
27. Baliga BR, Patankar SV (1988) Elliptic systems: finite element I. In: Minkowycz WJ, Sparrow EM, Schneider GE, Plether RH (eds) Handbook of numerical heat transfer. Wiley, New York
28. Swaminathan CR, Voller VR, Patankar SV (1993) A streamline upwind control volume finite element method for modeling fluid flow and heat transfer problems. Finite Elem Anal Des 13:169–184
29. Li C, Zou Z, Duan Z (2000) Multiple isoparametric finite element method for nonhomogeneous media. Mech Res Commun 27(2):137–142
30. Kim JH, Paulino GH (2002) Isoparametric graded finite elements for nonhonogeneous isotropic and orthotropic materials. J Appl Mech 69:502–514
31. Carslaw HS, Jaeger JC (1959) Conduction of heat in solids. Clarendon, Oxford
32. Ootao Y, Tanigawa Y (2004) Transient thermoelastic of functionally graded thick strip due to nonuniform heat supply. Compos Struct 63:139–146
33. Ching HK, Yen SC (2006) Meshless local Petrov–Galerkin analysis of 2D functionally graded strips under nonuniformly convective heat supply. Compos Struct 73:381–393
34. Zienkiewicz OC, Taylor RL (1989) The finite element method: volume 1 basic formulation and linear problems, 4th edition. McGraw-Hill, NY
35. Vessakosol P, Charoensuk J (2010) Numerical analysis of heat transfer and flow field around cross-flow heat exchanger tube with fouling. Appl Therm Eng 30:1170–1178